



HAL
open science

Hybrid Multimodal Contrast Agent for Multiscale In Vivo Investigation of Neuroinflammation

Szilvia Karpati, Violaine Hubert, Ines Hristova, Frederic Lerouge, Frédéric Chaput, Yann Bretonnière, Chantal Andraud, Akos Banyasz, Guillaume Micouin, Maelle Monteil, et al.

► **To cite this version:**

Szilvia Karpati, Violaine Hubert, Ines Hristova, Frederic Lerouge, Frédéric Chaput, et al.. Hybrid Multimodal Contrast Agent for Multiscale In Vivo Investigation of Neuroinflammation. *Nanoscale*, 2021, 10.1039/D0NR07026B . hal-03134034

HAL Id: hal-03134034

<https://hal.science/hal-03134034>

Submitted on 8 Feb 2021

HAL is a multi-disciplinary open access archive for the deposit and dissemination of scientific research documents, whether they are published or not. The documents may come from teaching and research institutions in France or abroad, or from public or private research centers.

L'archive ouverte pluridisciplinaire **HAL**, est destinée au dépôt et à la diffusion de documents scientifiques de niveau recherche, publiés ou non, émanant des établissements d'enseignement et de recherche français ou étrangers, des laboratoires publics ou privés.

Hybrid Multimodal Contrast Agent for Multiscale *In Vivo* Investigation of Neuroinflammation

Szilvia Karpati^a, Violaine Hubert^b, Inès Hristovska^c, Frédéric Lerouge^{a*}, Frédéric Chaput^a, Yann Bretonnière^a, Chantal Andraud^a, Akos Banyasz^a, Guillaume Micouin^a, Maëlle Monteil^d, Marc Lecouvey^d, Marion Mercey-Ressejac^e, Arindam Dey^e, Patrice N. Marche^e, Mikael Lindgren^f, Olivier Pascual^c, Marlène Wiart^b, Stephane Parola^{a*}

a Université de Lyon, Ecole Normale Supérieure de Lyon, CNRS UMR 5182, Université Lyon 1, Laboratoire de Chimie, 46 allée d'Italie, F69364 Lyon, France

b Univ-Lyon, CarMeN laboratory, Inserm U1060, INRA U1397, INSA Lyon, Université Claude Bernard Lyon 1, F-69600, Oullins, France

c Institut NeuroMyoGène, Université Claude Bernard Lyon 1, CNRS UMR 5310, INSERM U1217, Université Lyon, Villeurbanne 69100, France

d Université Sorbonne Paris Nord, Laboratoire CSPBAT, CNRS UMR 7244, F-93017 Bobigny Cedex, France

e Institute for Advanced Biosciences, Université Grenoble-Alpes, INSERM U1209, CNRS UMR5309, La Tronche, France.

f Norwegian University of Science and Technology - Department of Physics, Høgskoleringen 5, Realfagbygget, 7491 Trondheim, Norway

* corresponding author

Abstract

Neuroinflammation is a process common to several brain pathologies. Despite its medical relevance, it still remains poorly understood; there is therefore a need to develop new *in vivo* imaging strategies to monitor inflammatory processes longitudinally. We here present the development of a hybrid imaging nanoprobe named **NP3**, that was specifically designed to get internalized by phagocytic cells and imaged *in vivo* with MRI and bi-photon microscopy. **NP3** is composed of a 16 nm core of gadolinium fluoride (GdF₃), coated with bisphosphonate polyethylene glycol (PEG) and functionalized with a Lemke-type fluorophore (LEM-A). It has a hydrodynamic diameter of 28±8 nm and a zeta potential of -42±6 mV. The MR relaxivity ratio at 7T is $r_1/r_2 = 20$; therefore, **NP3** is well suited as a T₂/T₂* contrast agent. *In vitro* cytotoxicity assessments performed on four human cell lines revealed no toxic effects of **NP3**. In addition, **NP3** is internalized by macrophages *in vitro* without inducing inflammation or cytotoxicity. *In vivo*, uptake of **NP3** has been observed in the spleen and the liver. **NP3** has a prolonged vascular remanence, which is an advantage for macrophage uptake *in vivo*. The proof-of-concept that **NP3** may be used as a contrast agent targeting phagocytic cells is provided in an animal model of ischemic stroke in transgenic CX3CR1-GFP/+ mice using three complementary imaging modalities: MRI, intravital two-photon microscopy and phase contrast imaging with synchrotron X-rays. In summary,

32 **NP3** is a promising preclinical tool for the multiscale and multimodal investigation of
33 neuroinflammation.

34 **Introduction**

35 Stroke is one of the leading causes of mortality worldwide accounting for 11.8% of global deaths.¹
36 Ischemic stroke is induced by transient or permanent occlusion of a cerebral artery.² The perturbation
37 of blood flow leads to neuronal death in the most severely hypoperfused areas. In addition, a complex
38 sequence of inflammatory events occurs following ischemic stroke, among which the activation of
39 infiltrating and brain resident macrophages (microglia).³ This neuroinflammatory response may lead to
40 secondary brain damage and thus represents a potential therapeutic target. However, the complex role
41 of neuroinflammation is not well understood to date. There is thus a need to develop new *in vivo*
42 preclinical imaging strategies to follow inflammatory processes longitudinally at the acute stage of
43 ischemic stroke, in order to better understand the pathophysiology, as well as to monitor the effects of
44 anti-inflammatory treatments prior to their clinical translation.

45 Today, PET imaging of microglia activation using 18 kDa translocator protein (TSPO) tracers is at the
46 forefront for translational in-vivo molecular imaging of neuroinflammation following stroke.⁴ One
47 limitation of this approach, however, is that at the acute stage of ischemic stroke (<72h), the number
48 of activated microglia is below the limit of detection. Therefore currently PET imaging cannot be used
49 to monitor neuroinflammation in this crucial time-window, where immunomodulatory treatments may
50 be the most effective. The noninvasive nature of MRI and CT, in conjunction with their wide availability,
51 make them particularly suitable for longitudinal neurologic imaging studies. Magnetic resonance
52 imaging (MRI) or computed tomography (CT) coupled with the administration of metallic nanoparticles
53 (such as iron oxides) represents an attractive tool for studying inflammation.^{5,6} After their intravenous
54 injection, the nanoparticles get internalized by activated phagocytic cells, mostly macrophages. Since
55 phagocytic cells strongly participate in the development of inflammation processes, these imaging
56 approaches are used as a surrogate marker of inflammatory processes. The advantage of using metal-
57 based nanoparticles for this purpose is the possibility to combine complementary imaging modalities
58 at different scales to track the labelled macrophages. One of the limitations of these techniques,
59 however, is the fact that the signals seen on postcontrast images may have different origins than
60 nanoparticle-labelled cells, for instance microhemorrhages or microcalcifications. One way to address

61 this issue is to design contrast agents that may be imaged with element-specific imaging tools, for
62 instance fluorine for MRI⁷ and gadolinium for spectral photon counting CT.⁸ In addition, to further
63 validate the biological substrate of MR and CT signals, there is a need to complement these techniques
64 with imaging tools that are better resolved spatially and provide information about specific immune
65 cells. Intravital two-photon induced fluorescence imaging is a good candidate due to its high sensitivity,
66 resolution at sub-cellular scale, the possibility of real-time monitoring and the availability of transgenic
67 mice such as CX3CR1-GFP/+ mice that have green fluorescent microglia and macrophages.⁹

68 Consequently, the aim of our study was to design a multimodal contrast agent adapted simultaneously
69 for three imaging modalities (MRI, CT and two-photon microscopy) and optimized for the passive
70 targeting of phagocytic cells. In addition, because our primary application is ischemic stroke, we added
71 the specification that our imaging probe should be able to cross the blood brain barrier (BBB) following
72 focal cerebral ischemia. Nanoparticles are well-suited for this aim because they circulate longer than
73 small molecular weight contrast agent and hence can accumulate in inflammatory regions with high
74 phagocytic activity. Because gadolinium is particularly well-suited for both MRI and spectral photon
75 counting CT [2], we here propose to use functionalized gadolinium fluoride (GdF₃) nanoparticles as a
76 contrast platform.

77 Due to its very low solubility (less than $3 \cdot 10^{-5}$ mol L⁻¹) in aqueous media,¹⁰ GdF₃ is considered as one of
78 the most stable gadolinium compounds. Moreover, nanostructured materials concentrate a high
79 amount of gadolinium ions, giving rise to high contrast-to-noise ratio both in MRI and CT. Recently, we
80 demonstrated that GdF₃ nanoparticles were optimal for *in vivo* angiography with spectral photon
81 counting CT, due to their efficient X-ray attenuation properties and long vascular remanence.¹¹

82 In the present work, size and coating of the GdF₃ platform were finely tuned to allow the passive
83 targeting of phagocytic cells. The probe was further functionalized with a dedicated two-photon
84 microscopy fluorophore. This paper reports the synthesis and characterization of this novel imaging
85 nanoprobe. We verified that the nanoprobe was internalized *in vitro* by bone-marrow derived
86 macrophages. We provide data on cytotoxicity as well as *in vivo* biodistribution and pharmacokinetic.
87 Finally, the proof-of-concept of its potential for multiscale and multimodal imaging of
88 neuroinflammation was obtained in a murine model of ischemic stroke using three complementary

89 imaging modalities: MRI, intravital two-photon microscopy and phase contrast imaging with
90 synchrotron X-rays.

91 **Experimental**

92 **Synthesis of NP1**

93 4.83 g (0.013 mol) of GdCl₃·6H₂O (Alfa Aesar 99.9%) was stirred at room temperature in 2 mL of
94 ethylene glycol (EG) until complete dissolution and was further diluted with 3 mL of 2-pyrrolidinone.
95 This solution was added to a solution of 1.1 mL (0.0316 mol) 50% hydrofluoric acid in 24 mL of 2-
96 pyrrolidinone. The mixture was then heated up to 170°C for 1.5 h in a 50 mL stainless steel Teflon lined
97 digestion pressure vessel. The obtained suspension was cooled down to room temperature and the
98 particles were precipitated in acetone. The colloidal nanoparticles were purified by several
99 centrifugation-redispersion cycles using methanol as washing solvent. After purification, the
100 nanoparticles were suspended in water and freeze-dried for further use.

101 **Synthesis of NP2 and NP3**

102 First step: 600 mg of GdF₃ NP were suspended in 2 mL of ultrapure water. To this suspension was added
103 a solution of a mixture of two types of bifunctional bisphosphonate-terminated PEGs in water: 40.3 mg
104 (4.67 10⁻⁵ mol; 5mol% of total ligand quantity) of **2** and 899 mg (8.87 10⁻⁴ mol) of **1** in 2 mL of ultrapure
105 water. The homogeneous suspension was magnetically stirred at 80°C for 2h and stirred at room
106 temperature for one night. The as prepared functionalized nanoparticles **NP2** were subjected to dialysis
107 for one week to remove excess ligand and then were freeze-dried. In a second step a suspension of **NP2**
108 (452 mg in 1.5 mL of water) was added to a solution of **3** (5.5 mg) in ethylene glycol (6.5 mL). The
109 mixture was heated to 150°C and stirred for 5h. The obtained fluorescent and coated NPs (**NP3**) were
110 first precipitated in acetone, washed with ethanol, and centrifuged several times, until the supernatant
111 becomes colorless.

112 **Analysis of particle morphology and composition**

113 DLS and Zeta potential measurements were performed on aqueous suspensions of the particles, by a
114 Malvern Instruments Nano ZS. XPS analysis was carried out by PHI Quantera SXM instrument, with
115 monochromatic Al K α source. TEM images were acquired using a JEOL JEM 1400 equipped with a Gatan
116 Orius 600 camera and operated at 120kV. XPS measurements were carried out with a PHI Quantera

117 SXM photoelectron spectrometer using Al K α radiation ($h\nu$ 1486.7 eV). MultiPak software was used for
118 the fitting procedure.

119 **Two-photon absorption spectroscopic study**

120 For two-photon spectroscopic study the excitation source was a tunable femtosecond Ti-sapphire laser
121 (Chameleon Ultra I, Coherent) producing 140 fs pulses. The excitation beam was focused by a 100 mm
122 focal length lens into a 10x10 mm spectroscopic quartz (QZS) cell containing the sample. The emitted
123 fluorescence was collected at right angle and delivered to a spectrometer (AvaSpec-EVO, Avantes) via
124 an optical fiber. The cell position was adjusted so that the optical path was minimized in the cell on
125 both the excitation and the detection side; this allowed reducing artefacts due to inner-filter effects
126 and scattering. Additionally, low-pass filters were used between the cell and the entrance of the fiber
127 to prevent the scattered laser light from entering the spectrometer as much as possible. Here
128 fluorescein in a pH 13 aqueous solution was used as the two-photon reference standard.¹²

129 **Cytotoxicity assays**

130 Cell Lines: **NP3** nanoparticle potential cytotoxicity was assessed on four human cell lines, all supplied
131 by the American Type Culture Collection (ATCC). A549, epithelial-like cells from human lung, were
132 cultivated in DMEM 4.5 g L⁻¹ glucose + GlutaMAX medium supplemented with 10% fetal calf serum (FCS)
133 and 1% penicillin-streptomycin. THP-1, monocytes from human peripheral blood, were cultivated in
134 RPMI 1640 + GlutaMAX medium supplemented with 10% FCS, 1% penicillin-streptomycin, 1% pyruvate
135 and 4.5 g L⁻¹ glucose. HepG2, human hepatocytes, were cultivated in MEM + GlutaMAX medium
136 supplemented with 10% FCS, 1% penicillin-streptomycin and 1% pyruvate. Finally, HEK 293T, embryonic
137 kidney cells from human, were cultivated in the same medium than HepG2 cells. Cell Survival Assays:
138 **NP3** impact on cell lines was evaluated using two complementary assays: the LDH (Lactate
139 Dehydrogenase) assay, assessing cell membrane damages and the MTT (3-(4,5-[dimethylthiazol](#)-2-yl)-
140 2,5-di[phenyl](#)tetrazolium bromide) assay, assessing mitochondrial activity. Briefly, the different cell lines
141 were seeded in 96-well plates at 10⁵ cells/mL for A549, HEK and HepG2, and 5.10⁵ cells/mL for THP-1,
142 and incubated for 24h at 37°C and 5% CO₂. After 24h, cells were exposed to different **NP3**
143 concentrations (0.5 nM to 5000 nM). Cell survival assays have been performed at 48 hours and 72 hours
144 after **NP3** incubation. For LDH assay, cells were incubated with 100 μ L of CytoToxOne reagent for
145 10 minutes at 22°C. 50 μ L of Stop solution were then added in each well and cell death is measured by

146 fluorescence with ELISA plate reader (Victor, Perkin Elmer) at $\lambda_{\text{ex}} = 544 \text{ nm}$ and $\lambda_{\text{em}} = 572 \text{ nm}$. For MTT
147 assay, 10 μL of MTT Sigma-Aldrich solution (5 mg mL^{-1} in PBS) were added to each well, and the 96-well
148 plates were incubated for 2 hours at 37°C. 100 μL of lysis buffer (SDS 10%) were then added to each
149 well, and after 3 hours of agitation, cell viability was determined by absorption measurement
150 ($\lambda = 570 \text{ nm}$) with ELISA plate reader (Victor, Perkin Elmer).

151 **Animal model and *in vivo* experimental timeline**

152 All procedures involving animals and their care were carried out according to the European regulation
153 for animal use (EEC Council Directive 2010/63/UE, OJ L 276, Oct. 20, 2010). This study was approved by
154 our local ethic committee “Comité d’éthique pour l’Expérimentation Animale Neurosciences Lyon”
155 (CELYNE - CNREEA number: C2EA – 42).

156 At D0, transgenic CX3CR1-GFP/+ mice expressing green fluorescent protein (eGFP) in
157 microglia/macrophages were subjected to a model of ischemic stroke (males, n=4). Permanent
158 occlusion of the distal middle cerebral artery (pMCAo) was induced in the anesthetized (isoflurane, 2%,
159 ISO-VET, Piramal Healthcare, Morpeth, UK) animals, using the application of iron chloride (10% FeCl_3)
160 solution, according to the procedure described previously by Karatas et al.¹³ One mouse not submitted
161 to pMCAo served as control. One day after the occlusion (D1), all the mice (n=5) underwent a basal MRI
162 session to assess the presence of an ischemic lesion. Immediately after, the mice were injected into the
163 tail vein with 2 mmol kg^{-1} of **NP3** (n=5). Following the injection, a subgroup of mice (pMCAo mouse,
164 n=2; control mouse; n=1) was submitted to a second surgical intervention for intravital two-photon
165 microscopy imaging: after the skull was thoroughly thinned, a 6 mm diameter polyamide (MRI-
166 compatible) implant was placed over an area encompassing both the ischemic lesion and some
167 extralesional tissue. On the same day (D1), these mice underwent a 2 hours-two-photon excitation
168 microscopy (TPEM) imaging session. In order to have pre-**NP3** and post-**NP3** TPEM images, the control
169 mouse was intravenously injected with **NP3** during the TPEM session and was also imaged 24 hours
170 after **NP3** injection (D2). To assess the potential of TPEM for **NP3** longitudinal follow-up, one of the pMCAo
171 mice was submitted to a second TPEM imaging session. Finally, all mice (n=5) underwent a post-**NP3**
172 MRI session 48 hours following **NP3** injection (D3) and were then euthanized. *Ex vivo* X-ray phase
173 contrast imaging was performed on the brain of pMCAo mouse.

174 ***In vitro* and *in vivo* MRI**

175 All the MRI exams were performed on a 7T horizontal-bore Bruker Advance II rodent imaging system
176 (Bruker Biospin, Ettlingen, Germany). For the *in vivo* MR imaging exams, mouse anaesthesia was
177 induced with a mixture of air and 3.5% isoflurane and maintained with 2% isoflurane. The animals were
178 placed in an MRI-compatible mouse cradle, and the body temperature was monitored thanks to
179 circulating heated water. Relaxivity measurements: To quantify the r_1 and r_2 relaxivities of **NP3** (in mM^{-1}
180 s^{-1}), phantoms have been prepared with a range of twelve gadolinium concentrations going from 0 to
181 5 mM in saline. To reach the appropriate concentrations, **NP3** phantoms were prepared using a 0.5 M
182 stock solution dissolved in saline. Measurements were then performed at 25°C. T_1 maps were obtained
183 from a fast imaging with steady-state procession (FISP) sequence (TE/TR=2.1/4.2 ms; Inversion time
184 (TI): 73.8 ms; 32 echoes) by fitting an inversion/recuperation function to the data. T_2 maps were
185 obtained from a multiple spin-echo sequence (MSME; TE [interecho delay]/TR=50/5000 ms; 24 echoes)
186 by fitting a monoexponential function to the data. Biodistribution and pharmacokinetic: To evaluate
187 **NP3** biodistribution and pharmacokinetic, C57Bl/6 mice (males, n=4) were imaged using a 35 mm inner
188 diameter whole-body transmit-receive coil for signal acquisition. To avoid movement artifacts due to
189 the breathing, the acquired sequence was triggered on mouse respiratory rhythms. Abdominal axial T_1
190 images were obtained with a dynamic RARE 2D sequence (TE/TR = 7.51/960.77 ms; FA = 90; number of
191 averages = 2; acquisition time 1.32 min; number of repetitions = 25). 37 slices were acquired from the
192 top of the heart to the bottom of the liver, using a FOV of $35 \times 35 \text{ mm}^2$, a slice thickness of 1 mm and a
193 matrix of 128×128 . **NP3** (2.0 mmol kg^{-1}) was injected as a bolus *in vivo* in the magnet between the
194 second and the third repetitions. MR signal changes in time were analyzed in regions of interest (ROI)
195 and normalized using pre-contrast values. Imaging of stroke-induced animals: A 50 mm inner diameter
196 birdcage coil was used for transmission and a 15 mm diameter surface coil was used for reception. The
197 following axial sequences were used: a spin-echo T_2 -weighted image (T_2 -WI), TE/TR = 43.8/5000 ms,
198 bandwidth = 40 kHz, number of averages = 6, acquisition time 12 min; a T_2 -star gradient-echo (GRE)
199 FLASH sequence (T_2^* -WI), TE/TR= 6/750 ms, bandwidth= 40 kHz, flip angle (FA)= 20°, number of
200 averages = 8, acquisition time 19 min. For each sequence, 25 slices were acquired from the olfactory
201 bulb to the cerebellum of the mice, using a field of view (FOV) of $20 \times 20 \text{ mm}^2$, a slice thickness of 500 μm
202 and a matrix size of 256×256 .

203 **Two-photon excitation microscopy (TPM)**

204 For the *in vivo* TPEM imaging sessions, mice have been anesthetized with a mixture of ketamine
205 (100 mg kg⁻¹) and medetomidine (1 mg kg⁻¹). Their body temperature was maintained at 37 °C using a
206 heating pad. TPEM observations were performed on a Bruker Ultima microscope (Insight 3X laser,
207 Spectra Physics), equipped with a 20x water-immersion objective (0.95 N.A. Olympus). Green (CX3CR1-
208 GFP/+ cells) and red (**NP3** particles) fluorescence were separated by a 560 nm dichroic mirror coupled
209 to 525/50 nm and 650/40 emission filters.

210 30-45 consecutive Z-stacks were acquired at a depth of 50-150 μm, with a step size of 1 μm and a
211 resolution of 521x521 pixels. ImageJ and Icy (open source software created by BioImage Analysis Lab,
212 Institut Pasteur, France; <http://icy.bioimageanalysis.org/>) were used for image treatment, and drift
213 correction was applied with a custom-written Matlab software (used for image correction for drift
214 during the acquisition).

215 **X-ray phase contrast tomography**

216 For *ex vivo* phase contrast tomography, mice have been euthanized by intracardiac perfusion with 4%
217 PFA. Brains were then extracted and dehydrated in successive ethanol baths. In-line phase contrast
218 tomography was performed on beamline ID17 of the European Synchrotron Radiation Facility (ESRF) in
219 Grenoble at 26 keV. An indirect detection-based detector with a LuAg scintillator, standard microscope
220 optics and a 2048x2048 pixel CCD camera was positioned 3 m from the sample to obtain phase contrast.
221 The whole-brain data set was acquired at an isotropic pixel size of 7.5 μm. Acquisition time of the 3000
222 projections was <5 minutes per brain. Reconstruction was performed with Paganin algorithm by setting
223 γ/β to 1000 as in.¹⁴

224 **Results and Discussion**

225 **Nanoparticle core synthesis (NP1)**

226 The synthesis of the GdF₃ inorganic core (**NP1**) was adapted from a previously described method¹¹
227 under solvothermal conditions in a mixture of ethylene glycol (EG) and 2-pyrrolidinone.¹⁵⁻¹⁷ The
228 originality of this method consists in the generation of various complexes involving F⁻ and Gd³⁺ ions
229 (Scheme 1A) leading to an improved control of nanoparticle morphology and size distribution. As shown
230 by transmission electron microscopy (TEM) observations (Fig. S1-A), **NP1** are spheroidal and slightly
231 elongated. Their hydrodynamic diameter determined by dynamic light scattering (DLS) measurements

232 (Fig. S1-B) is 16 ± 5 nm, with low polydispersity (polydispersity index, PDI: 0.16). The X-ray powder
233 diffraction (XRPD) pattern (Fig. S1-C) shows high crystallinity of **NP1** and comparison of the peaks to the
234 reference pattern ICSD Card 00-012-0788 demonstrates the pure orthorhombic phase (*Pnma* space
235 group) of GdF_3 . The positive zeta potential $+45\pm 10$ mV measured for **NP1** in water, suggests an excess
236 of Gd^{3+} ions on the surface, which is in accordance with the observed 67.7 atomic % of gadolinium,
237 determined by X-ray photoelectron spectroscopy (XPS) analysis (Table S1). Furthermore, this elemental
238 composition analysis reveals a F/Gd atomic ratio of 0.39 at the surface. Such small ratio (expected F/Gd
239 ratio is 3) is explained by two aspects. First, the surface composition of a nanoparticle is always different
240 from the bulk composition (surface effects, crystal defects etc.) and segregation of elements is
241 frequently observed.¹⁸ XPS is a surface scanning technique, with a penetration depth of a few
242 nanometers. In our case it was approximately 3 nm, therefore the observed composition was not the
243 composition of bulk GdF_3 . The second reason is that in our synthesis conditions F/Gd is kept lower than
244 the stoichiometric ratio, because F^- excess induces in the case of gadolinium a mixture of two crystalline
245 phases: orthorhombic and hexagonal. However, as it was mentioned before, according to X-ray powder
246 crystallographic measurements, the overall crystalline phase corresponds effectively to the
247 orthorhombic GdF_3 phase (Fig S1-C). According to attenuated total reflection Fourier-transform
248 infrared spectroscopy (ATR-FTIR) measurements, small organic capping molecules identified as the
249 open form of solvent molecule 2-pyrrolidinone, are present on the surface (Fig. S2-A).

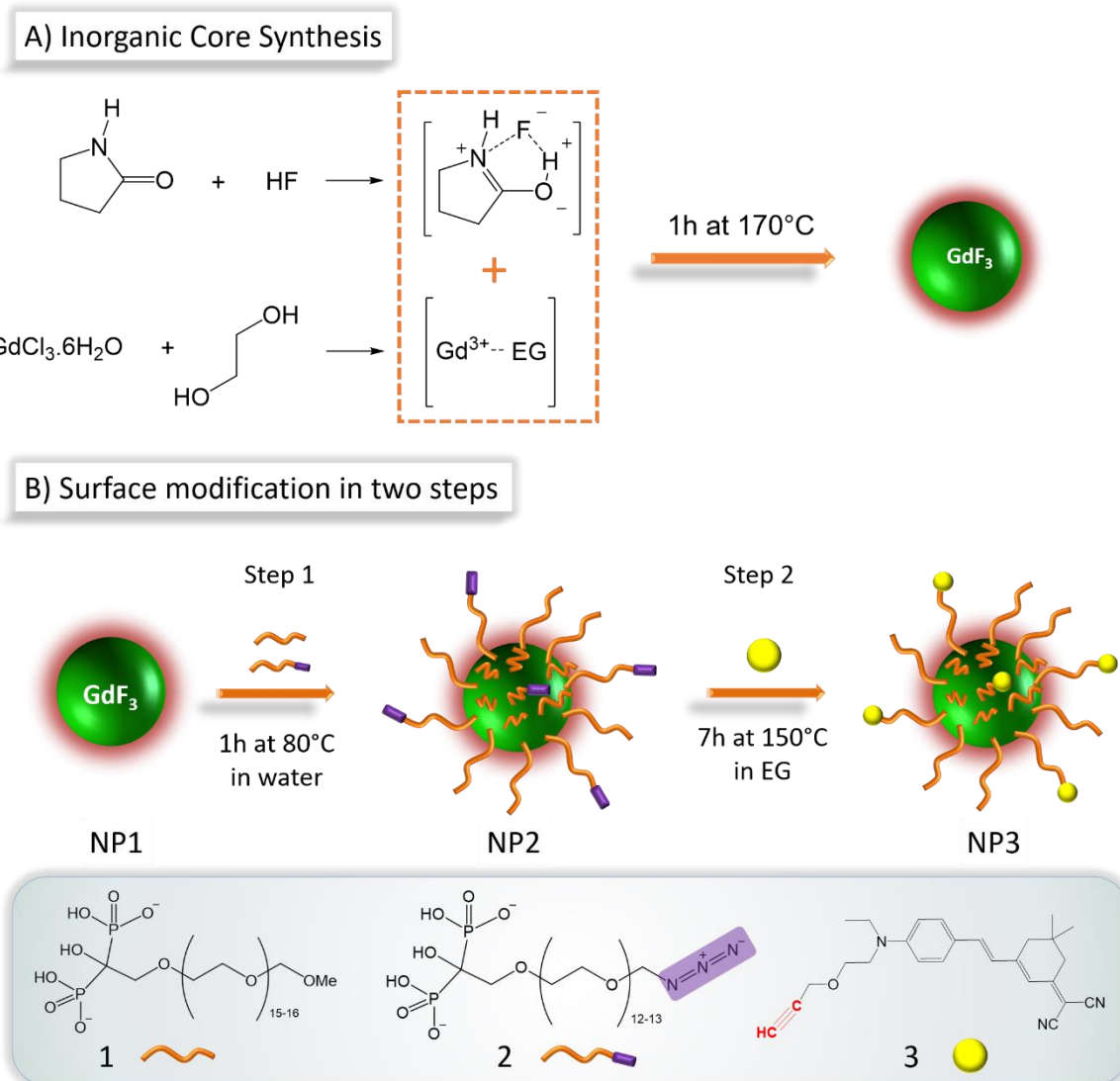
250

251 **Core-shell nanoparticles (NP2)**

252 The surface modifications of **NP1** was achieved following a two-step approach presented in Scheme 1-
253 B. The first step consists in the preparation of functional particles **NP2**, through the grafting of a mixture
254 of two bisphosphonate PEG derivatives with and without azide reactive groups (compounds **1** and **2**,
255 respectively). The synthesis of these ligands developed by Lecouvey *et al.* has been described in detail
256 elsewhere.¹⁹ The bisphosphonate functions allow strong anchoring via multidentate chelation of
257 gadolinium ions.^{20,21} While ligand **1** is used to ensure biocompatibility, **2** allows coupling with the
258 fluorophore **3** through its $-N_3$ group. The molar percentages of ligand **1** and ligand **2** were set at
259 respectively 95% and 5%. This ratio was optimized taking into consideration the stability of the particle
260 in biological media and the optical properties for appropriate two-photon fluorescence imaging. The
261 second step focuses on the coupling of fluorophore **3** (the synthesis of **3** is described in ref.²²) with the

262 azide functions on the PEG-coated nanoparticle **NP2**.

263



264

265 **Scheme 1 A)** Solvothermal synthesis of GdF_3 nanoparticles (**NP1**). The solvent, 2-Pyrrolidinone is complexing the fluoride
266 ion (source of fluoride is HF) and ethylene glycol chelates Gadolinium (III) ions (from $GdCl_3$). The mixture is heated to $170^\circ C$
267 for 1h in a Teflon lined autoclave to give **NP1** nanoparticles. **B)** The surface of **NP1** is modified in two steps: first, PEG-ligands,
268 **1** and **2** are grafted and chromophore **3** is coupled in a second step.

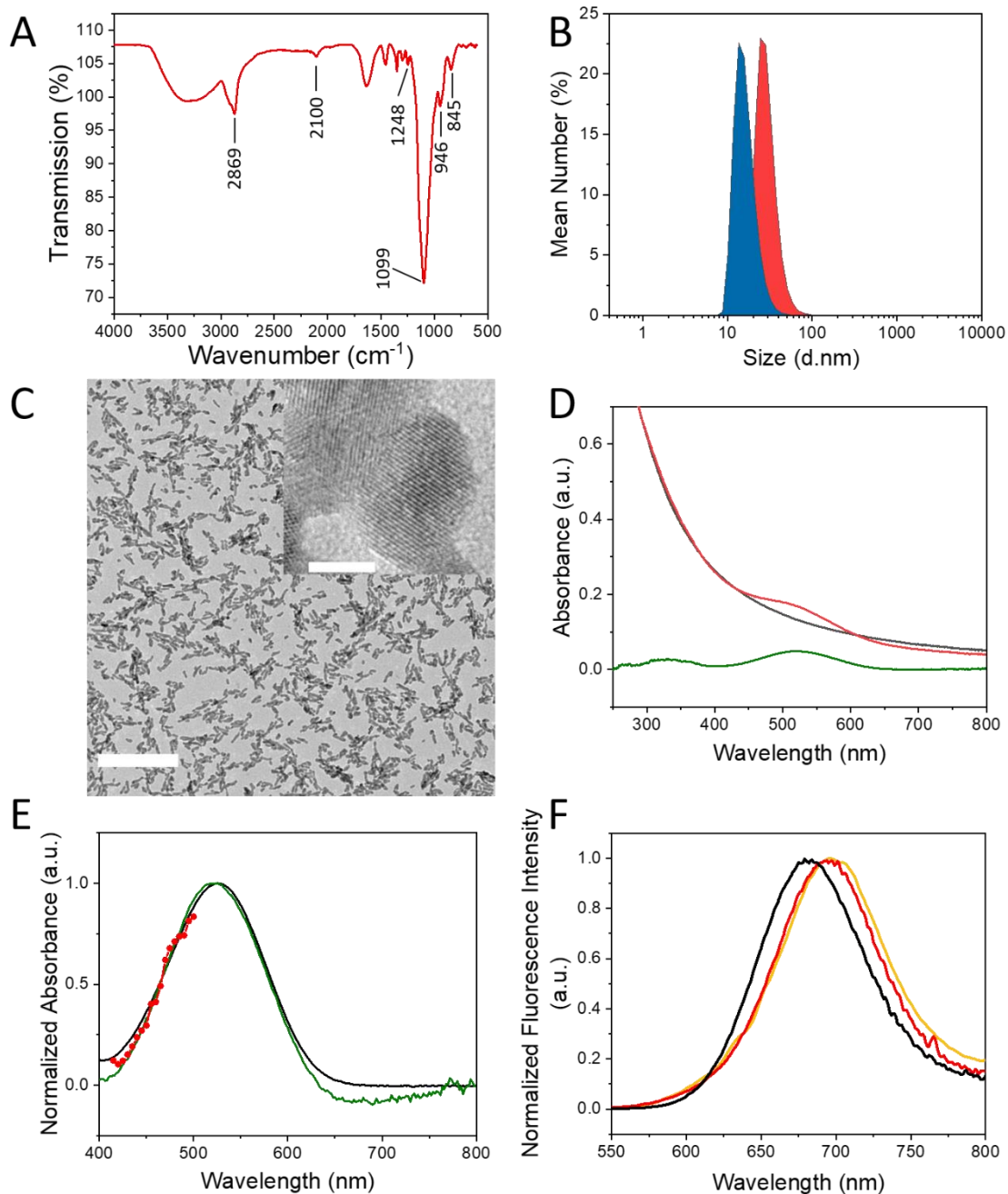
269

270 The success of multifunctional PEG grafting was first evaluated by ATR-FTIR spectroscopy. Infrared
271 spectrum of **NP2** (Fig. 1-A) as compared to **NP1** (Fig. S2-A, red spectrum) shows typical signatures of
272 PEG species, with bands at 2869 cm^{-1} and around 1100 cm^{-1} for ether C–H and C–O–C stretching modes
273 respectively.²³ The presence of the organic layer around the particles was also evidenced by DLS (Fig. 1-
274 B) where hydrodynamic diameter increases from $16\pm 5\text{ nm}$ (blue signal) to $21\pm 7\text{ nm}$ (red signal). Charge

275 surface of the particles was evaluated with zeta potential measurements, showing a switch from a
276 positive (+45±10 mV) to a negative value (−28±3 mV) due to the deprotonated bisphosphonate
277 moieties linked to surface gadolinium atoms. Grafting of PEG-ligands **1** and **2** on the particle was also
278 evidenced by thermogravimetric analysis (TGA) (Fig. S2-B) where a significantly higher weight loss
279 (29.3 %) corresponding to organics was observed in the case of **NP2** compared to **NP1**.

280 **Fluorophore coupling to NPs (NP3)**

281 One of the principal requirements for two-photon fluorescence imaging of biological media is that the
282 dyes emit fluorescence in the red-near infrared (NIR) spectral range, where the autofluorescence from
283 the medium is minimal and light is less scattered. The Lemke-type²⁴ fluorophore **3**, used in the present
284 work was specifically designed for fluorescence imaging in biological media. As previously reported, this
285 type of molecule was characterized by a strong dipolar donor-acceptor push-pull structure, which
286 induces favorable optical spectroscopic properties suitable for imaging in the first biological
287 transparency window (700-1000 nm).^{22,25,26} Coupling of **3** with **NP2** was performed without use of
288 copper catalyst, via thermally induced Huisgen-type 1,3-cycloaddition²⁷ to obtain **NP3**. Thermal
289 activation of the reaction was preferred here to avoid use of toxic copper(II) ions for *in vivo* application.
290 This coupling occurs between the azide functions on the surface of **NP2**, and the alkyne functions of
291 fluorophore **3**, resulting in a strong bonding through imidazole cycle. In order to confirm the
292 fluorophore grafting on **NP3**, infrared spectroscopy was used (Fig. S3-A). The vibration bands of PEG
293 moieties (2869 cm⁻¹ and 1100 cm⁻¹) and BP end-groups (1248 cm⁻¹ around 1099 cm⁻¹, 946 cm⁻¹ and
294 845 cm⁻¹ for P=O, P–O and P–O(H) stretching vibrations respectively)^{15,28} remain unchanged while the
295 one corresponding to –N₃ groups (2100 cm⁻¹) disappears along with the reaction advancement (Fig. S3-
296 A inset), clearly evidencing the coupling with **3**.



297

298 **Fig. 1 A)** FTIR-ATR spectra of **NP2** nanoparticles. **B)** DLS measurements of the particles before (**NP1**) any surface modification
 299 (blue) and after PEGylation and fluorophore grafting (**NP2**) (red). **C)** TEM image of the particles after surface modification
 300 (**NP3**). Scale bar is 50 nm for larger image and 5 nm for the inset. **D)** Absorption spectra of **NP3** (red line) and **NP2** (black
 301 line) are compared. The difference of these two spectra (green line) reveals the absorbance of the chromophore without
 302 the scattering due to the particles. **E)** Differential absorbance (green) showing the absorption bands of the chromophore
 303 (520 and 326 nm) compared to the spectrum of compound **3** in ethylene glycol (black line). The normalized two-photon
 304 absorption spectrum (red line+scatter) is reported on the same figure. for comparison. **F)** Normalized fluorescence emission
 305 spectra upon one photon excitation of free dye (compound **3**, black line) in methanol and **NP3** nanoparticles (red line)
 306 suspended in water. Upon excitation at 510 nm, the maximum emission values are 658 and 682 nm, respectively. The two-
 307 photon fluorescence spectrum obtained upon 1000 nm excitation of aqueous dispersion of **NP3** is indicated in dark yellow.

308

309 Interestingly, in spite of water-insolubility of **3**, the purified nanoparticles **NP3** were perfectly
310 dispersible in aqueous medium, resulting in a pale pink-color homogeneous colloidal suspension. DLS
311 measurements of **NP3** showed a slight increase in the average hydrodynamic size (28 ± 8 nm) due to the
312 presence of the polymeric coating. The measured Zeta-potential value is -42 ± 6 mV. The high stability
313 of the particles is thus explained by both electrostatic and steric interactions. The authors attribute zeta
314 potential decrease from -28 ± 3 mV (**NP2**) to -42 ± 6 mV (**NP3**) to the modification of coordination modes
315 of bisphosphonate groups on the particle surface. The coordination of multidentate bisphosphonate
316 moiety, which is the anchoring function of the ligands seem to be reorganized due to the heat-
317 treatment during the coupling reaction. Increasing the proportion of not complexed P-O⁻ bonds lead to
318 the lower negative zeta potential. XPS analysis of the high-resolution spectrum centered on O 1s (Fig. S4
319 C2) supports this hypothesis. The measured binding energy band was decomposed to two contributions
320 with peak maxima at 532.21 eV (61.11%) and 530.70 eV (38.89%), which were attributed to O-Gd and
321 (H)O-P binding energies respectively. XPS elemental analysis (Table S1) reveal F/Gd ratios of 0.39 and
322 0.60 for **NP1** and **NP3** particles, respectively. The apparent Gd depletion is explained by partial shielding
323 of surface gadolinium ions, due to the presence of the organic ligands (12.2 at% of carbon atoms on
324 **NP3** compared to 0% on **NP1**) in the case of **NP3**. High-resolution XPS spectra (Fig. S4) show that the
325 binding energy of Gd 3d_{5/2} appears at 1187.8 eV for **NP1** and at 1188 eV for **NP3**. The peak Gd 4d_{5/2}
326 appears at 142.7 eV for **NP1** and at 143.4 eV for **NP3**, which are attributed to GdF₃ compound.²⁹ Upon
327 functionalization the peaks of Gd 4d are not significantly changed, suggesting, that the inorganic core
328 retains its composition. The peak F 1s was detected at 684. eV for **NP3**, which also corresponds to the
329 form GdF₃.²⁹

330 **NP2** was incubated with compound **3** in the usual conditions, without heating, in order to confirm
331 unambiguously that compound **3** is covalently bonded and not adsorbed through weak interactions
332 with PEG chains present on the surface. The resulting mixture was purified through centrifugation
333 cycles and analyzed by UV-visible absorption spectroscopy (Fig. S3-B). The resulting absorption
334 spectrum showed only the scattering profile of the particles and no absorption band associated to the
335 fluorophore was observed. This is consistent with the fact that **3** does not react without heating and
336 conversely the covalent bonding of the fluorophore to the particle surface was confirmed for **NP3**.
337 Finally, TEM observations were performed on **NP3** to verify the stability of the GdF₃ core during the
338 heating process, (Fig. 1-C). TEM images showed similar morphology size and shape, as the initial

339 particles.

340 **Linear spectroscopy characterization of NP3**

341 Before using **NP3** for *in vivo* experiments, the preservation of the optical properties of **3** when coupled
342 to the nanoparticle was evidenced by absorption and emission spectroscopy. The UV-visible spectrum
343 of **3** was recorded in three different solvents to evaluate the effect of environment polarity on spectral
344 properties (Fig. S5). In all three cases, a strong and structureless band appears between 400 and 650 nm
345 accompanied by a smaller intensity band at shorter wavelengths (from 250 to 400 nm). Peak maxima
346 are undergoing a slight shift due to solvatochromic effect, confirming that the fluorophore **3** is sensitive
347 to its environment. The absorption spectrum of **NP3** (Fig. 1-D) shows a band in the 450-600 nm range,
348 above the continuous scattering background created by the particles. To determine the exact position
349 of band maximum and be able to compare **NP3** with **3**, the absorption spectrum of **NP2** was subtracted
350 from **NP3** spectrum (Fig. 1-D). The resulting curve (green line) reveals the absorption profile observed
351 for **3** in the **NP3** environment, with a peak maximum value at 520 nm slightly red-shifted. This
352 demonstrates that after grafting on the particles, **3** is in a highly polar medium. Indeed, the subtracted
353 spectrum (green line) and the absorption of **3** dissolved in EG are similar (Fig. 1-E) in good agreement
354 with the fact that on the surface of the particle, **3** is surrounded by the PEG chains.

355 **Table 1** Relevant Spectroscopic properties of compound **3** in different solvents and **NP3** in water

	λ_{\max} (nm)	$\varepsilon(\lambda_{\max})$ (mM ⁻¹ cm ⁻¹)	λ_{em} (nm) ^a	$\Delta\bar{\nu}$ (cm ⁻¹) ^a	RQY ^a
3					
in DCM ^b	505	32800	634	4029	0.01
in ACN ^b	500	29200	653	4686	0.03
in MeOH ^b	507	37000	658	4527	0.12
NP3					
in H ₂ O	520	–	682	4568	0.03
scattering corrected ^c					0.13

356 ^a $\lambda_{\text{ex}} = 510$ nm, RQY: relative quantum yield; reference Erythrosine B ³⁰ in methanol (QY_{Ref} = 0.09)

357 ^b DCM: dichloromethane; ACN: acetonitrile; MeOH: methanol

358 ^c The absorption spectrum is corrected for scattering and the corrected absorbance value is used to determine the RQY.

359 Fluorescence emission and excitation spectra were recorded for fluorophore **3** in different solvents and
360 in water for **NP3**. The spectroscopic results were summarized in Table 1. As it is shown in Fig. S6,
361 fluorescence emission of **3** undergoes a positive solvatochromism (red-shifted maxima) upon increasing

362 solvent polarity; this is consistent with previous studies on similar dyes.²⁵ The maximum emission for
363 **NP3** (Fig. 1-F) is also in agreement with the solvent polarity dependence of the free dyes' series (positive
364 solvatochromism). Upon excitation at 510 nm of **NP3** in water, the maximum emission detected is
365 centered at 682 nm. It is very unlikely that the highly lipophilic fluorophore **3** is surrounded by water
366 molecules in the **NP3** configuration. Instead, the polar PEG chains on the particle surface offer a more
367 favorable environment, which is in accordance with the previous observations from absorption
368 spectroscopy (Fig. 1-E).

369 As mentioned before, absorbance of **NP3** is highly dominated by scattering. The absorbance value at
370 the excitation wavelength ($\lambda_{exc} = 510$ nm), used for relative quantum yield determination, results in an
371 apparent quantum yield of only 3 %. However, by considering the subtracted spectrum, without
372 scattering (Fig. 1-D, green line), a more realistic value of absorbance is obtained with a calculated
373 quantum yield of 13 %. This value is in accordance with the results found for **3** in polar solvents such as
374 methanol (Table 1), suggesting that the fluorescence of **3** is not altered upon the coupling to the
375 particle.

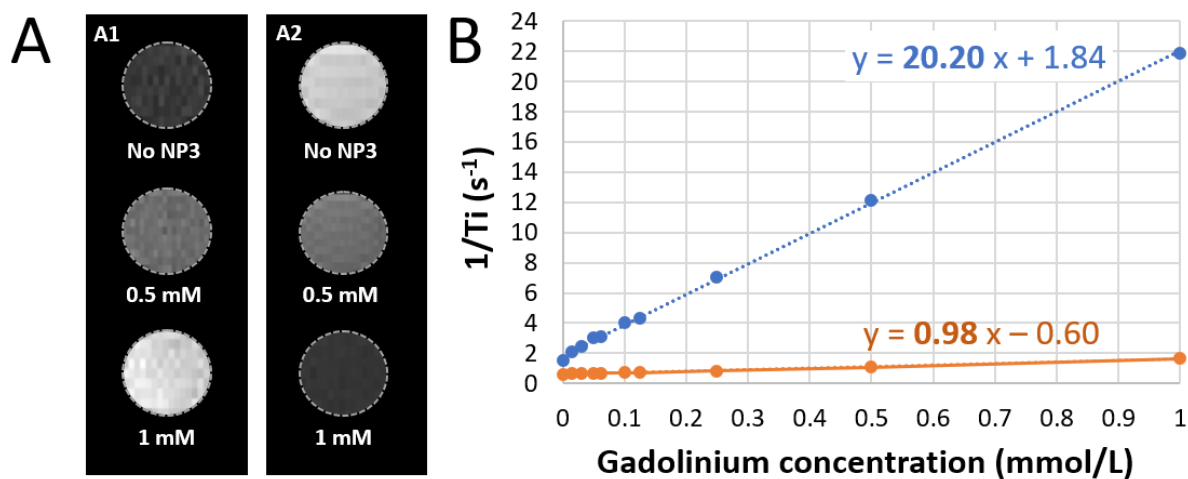
376 **Two-photon absorption (TPA) spectroscopic characterization of NP3**

377 Two-photon spectroscopic properties of **NP3** were evaluated prior to *in vivo* two-photon microscopy
378 imaging. Characterization of the two-photon absorption (TPA) cross sections of **NP3** at different
379 wavelengths was performed by measuring the two-photon induced excitation spectrum^{31,32} and
380 comparison to a known reference. The TPA spectrum of **NP3** was determined between 830 and
381 1000 nm, the tuning range of the excitation source being limited to the maximum of 1000 nm.
382 Consequently, only the blue-side of the TPA spectrum is characterized. According to the absorption
383 spectrum corrected for scattering, the concentration of fluorophore **3** in **NP3** suspension used to
384 evaluate the TPA cross-section values (σ_{TPA}) is 16 μ M. At 980 nm, the excitation wavelength of our two-
385 photon microscopy experiments, the σ_{TPA} is approximately 30 GM. This value is significantly lower than
386 fluorophores of similar structures in solution.²⁶ This discrepancy is explained by the important decrease
387 of the excitation and emission intensity due to the high scattering induced by particles in our TPA
388 characterization configuration (see experimental details). For this reason, the normalized TPA spectrum
389 of **NP3** is presented in Fig. 1-E (red scatter+line) and not the absolute σ_{TPA} values. As previously
390 observed for the chromophore **3**,²⁵ this spectrum overlaps with the blue part of the linear absorption
391 of **NP3**.

392 The TPA-induced fluorescence spectrum of **NP3**, shown in Fig. 1-F (yellow line), matches well with its
 393 one-photon excited counterpart (Fig. 1-F, red line), showing that the fluorescence originates from the
 394 same excited state in both cases. This observation justifies the use of the fluorescence detection for the
 395 characterization of the TPA cross-section.

396 Magnetic resonance relaxivity measurements

397 T_1 and T_2 relaxation time values were determined at 7 T in saline and at room temperature from T_1 and
 398 T_2 maps (Fig. 2-A). The r_1 and r_2 relaxivities of **NP3** were calculated, using the following formulas: $1/T_1 = r_1 * C + 1/T_{1,0}$; $1/T_2 = r_2 * C + 1/T_{2,0}$ (T_1 and T_2 in seconds; C = molar concentration in mmol L^{-1} and $T_{1,0}$
 399 and $T_{2,0}$ are the relaxation times without contrast agent). A linear regression was made between the
 400 gadolinium concentration (mM) of **NP3** phantoms and the associated values $1/T_1$ or $1/T_2$. The slope of
 401 the line represents r_1 or r_2 ($\text{mM}^{-1} \text{s}^{-1}$), respectively (Fig. 2-B).



403

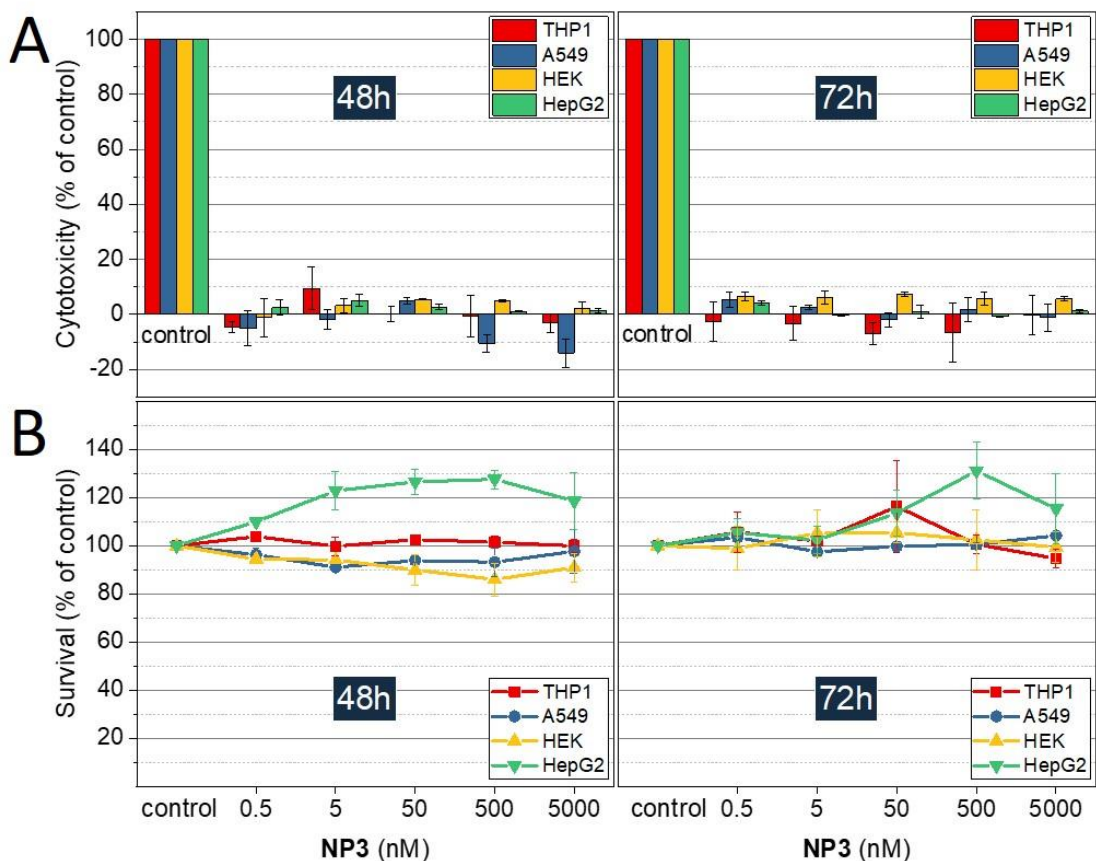
404 **Fig. 2 A) NP3** relaxivities. On T_1 -weighted images, MR signal increases with gadolinium concentration increase (A1) whereas
 405 on T_2 -weighted images, MR signal drops with the increase of gadolinium concentration (A2). **B)** Measurement of r_1 (orange)
 406 and r_2 (blue) relaxivities by linear regression connecting **NP3** phantoms gadolinium concentration to the value " $1/T_i$ ", where
 407 T_i means either T_1 or T_2 .

408 The estimated r_1 and r_2 relaxivities of **NP3** are $0.98 \text{ mM}^{-1} \text{ s}^{-1}$ and $20 \text{ mM}^{-1} \text{ s}^{-1}$, respectively, leading to a
 409 r_2/r_1 of 20.2. The r_2/r_1 value found here is close to the value observed for the ultrasmall
 410 superparamagnetic particles of iron oxide (USPIO), a well-known T_2/T_2^* MR contrast agent. Indeed, at
 411 the same magnetic field, the r_2/r_1 of the commercially available USPIO Ferumoxytol is 21.9.³³ Thus, **NP3**
 412 appears to possess promising T_2/T_2^* contrast properties at the concentrations that are expected *in vivo*

413 and was further evaluated *in vivo* using T₂ and T₂*-weighted MR sequences, in line with our previous
414 observations¹⁵

415 ***In vitro* cytotoxicity assessment**

416 Toxicity is a major concern regarding nanoparticles used in bioimaging and especially when *in vivo*
417 experiments are performed. In our specific case, prior to run *in vivo* imaging studies, the nanoparticle
418 **NP3** cytotoxicity was evaluated on several human cell lines: THP-1 monocytes, HepG2 hepatocytes,
419 A549 epithelial-like cells and HEK 293T kidneys cells. Two complementary assays, LDH and MTT, were
420 used to investigate the potential impact of **NP3** on both mortality and metabolic activity of the cells
421 incubated during 48h and 72h. The concentration of Gd in the culture medium ranges between 0 and
422 5 μM. All the LDH tests were compared to a positive control inducing 100% cell death. In all cases, the
423 percentage of specific cytotoxicity is below 10% regardless of the cell lines, the **NP3** concentration or
424 the incubation time (Fig. 3-A). In the case of the MTT assay, the metabolic activity of non-exposed cells
425 was taken as reference of the survival and/or the proliferation of the cells (100%); all cell lines show a
426 metabolic activity which remains constant, between 86 and 127%, independently of **NP3** concentration
427 (Fig. 3-B).



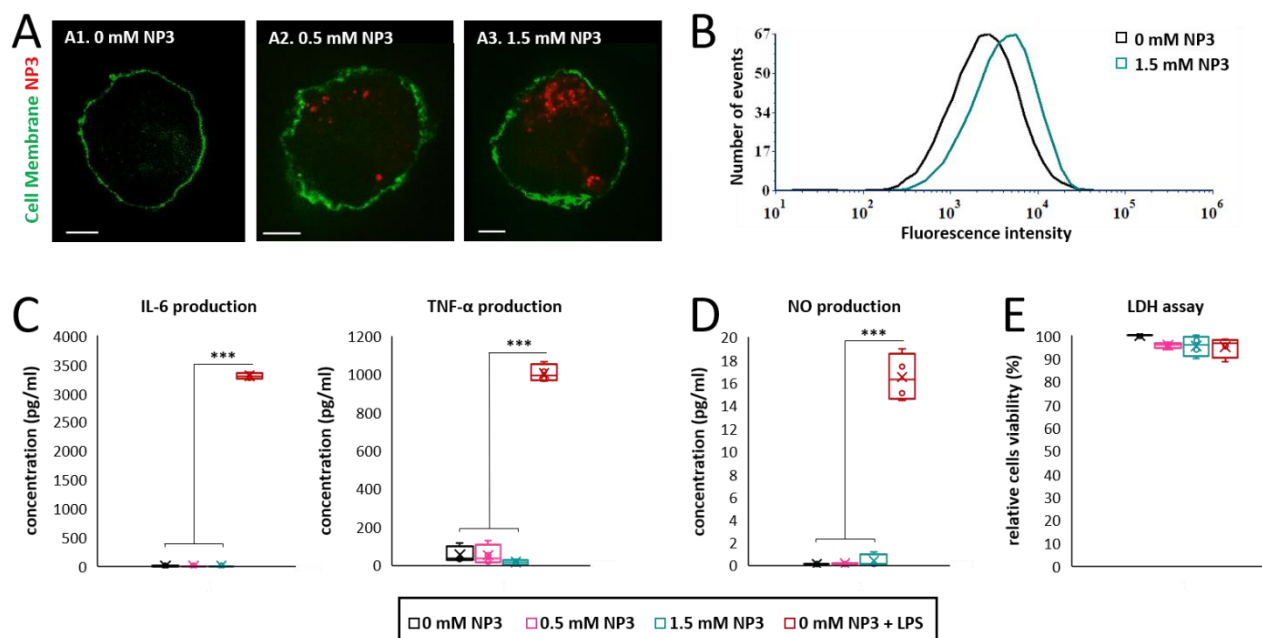
428

429 **Fig.3 Evaluation of NP3 cytotoxicity.** Cytotoxicity is measured in different human cultured cells: HepG2, HEK, A549 and
 430 THP1. Cells are incubated with 0-5 μM of NP3 for 48h and 72h. **A)** NP3 impact on cell survival assessed by LDH assay.
 431 "Control" corresponds to the positive control with 100% cell death. Mean \pm SD of duplicates. **B)** NP3 effect on cell viability
 432 assessed by MTT assay. Mean \pm SD of duplicates.

433 **NP3 is internalized by bone-marrow derived macrophages *in vitro* without overt toxic effects**

434 Internalization of NP3 particles by immune phagocytic cells was investigated *in vitro*. Bone marrow-
 435 derived macrophage (BMDM) primary cultures were incubated with NP3 particles for 24h (technical
 436 details are described in the *Supporting Material*). We first investigated the presence of the particle red
 437 fluorescent signal with confocal microscopy. The confocal images showed an important accumulation
 438 of nanoparticles inside the cells for 0.5 mM and 1.5 mM NP3 conditions (Fig. 4-A2 and 4-A3), but not in
 439 the control condition (Fig. 4-A1). NP3 internalization measured by flow cytometry supported these
 440 observations (Fig. 4-B). Pro-inflammatory cytokines, such as interleukine-6 (IL-6) and tumor-necrosis
 441 factor- α (TNF- α) play a key role in neuroinflammation. Therefore, we assessed their production by
 442 BMDM cultures exposed to NP3 particles and compared it to IL-6 and TNF- α production by non-
 443 exposed control BMDMs (Fig. 4-C). No significant difference has been observed for IL-6 and TNF- α

444 production by **NP3**-treated and non-exposed cells. By contrast, BMDM exposed to lipopolysaccharide
 445 or LPS (Fig. 4-C, red signal), used as a positive control for pro-inflammatory cytokine production, was
 446 associated with significantly higher concentrations of IL-6 and TNF- α . This observation suggests that
 447 **NP3** particles did not induce inflammation. In addition, BMDM exposure to **NP3** was not associated
 448 with increase of nitric oxide (NO) concentration (Fig 4D), thus suggesting that **NP3** did not induce
 449 oxidative stress either. Finally, cell viability was not affected by **NP3** exposure (Fig 4E).
 450

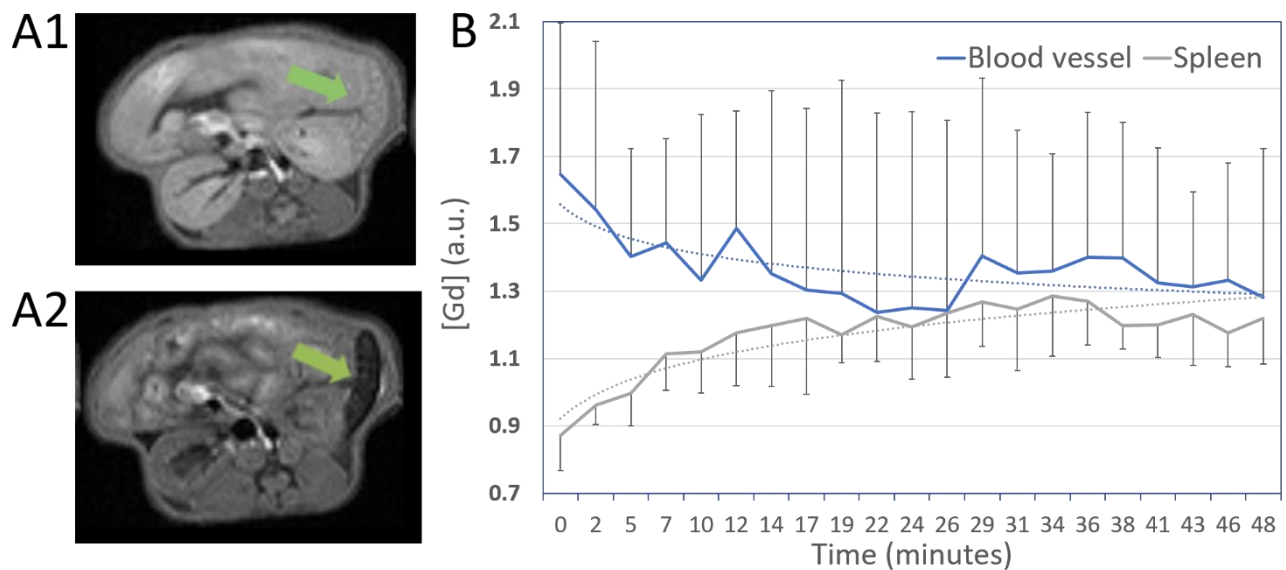


451 **Fig. 4 NP3 is internalized by BMDM and is not associated with cytotoxicity.** **A)** Confocal images of primary BMDM incubated
 452 with **NP3** (A2, 0.5 mmol/L; A3, 1.5 mmol/L) or without **NP3** (A1). BMDM cell membranes labelled with FITC conjugated
 453 cholera toxin are detected in green and **NP3** in red. (Scale bars: 5 μ m). **B)** Flow cytometer analysis shows the proportion of
 454 BMDM cells positives for **NP3** for BMDM incubated with 1.5 mmol/L **NP3**. BMDM cells not incubated with **NP3** (0 mM **NP3**)
 455 were used as control of **NP3** negative cells. **C)** Quantification of interleukin-6 (IL-6) and tumor-necrosis factor alpha (TNF- α)
 456 production by BMDM exposed to **NP3**. **D)** Quantification of nitric oxide production by macrophages exposed to **NP3**. **E)**
 457 Assessment of cell viability after exposition to **NP3**. For **C** to **E** experiments, cells exposed to LPS but not to **NP3** (condition
 458 "0 mM **NP3** + LPS") were used as a positive control of inflammatory environment. Significant differences calculated with a
 459 one-way ANOVA for n=4 independent experiments are indicated by *** for p < 0.005. w/o: without.
 460
 461

462 Altogether, these results (Fig. 3 and Fig. 4) demonstrate the lack of toxic effects of **NP3** on the fate of
 463 the cells, highlighting the high level of safety of these nanoprobe and confirming their potential to be
 464 used further for *in vivo* imaging of phagocytic cells.

465 **Biodistribution and pharmacokinetic profile of NP3**

466 Biodistribution and pharmacokinetic of **NP3** particles were evaluated *in vivo* in healthy mice by imaging
 467 the abdominal area with dynamic MRI. There was only a slight enhancement in the kidneys. In contrast,
 468 there was a strong accumulation of **NP3** in the spleen during the first hours after injection (Fig. 5-A),
 469 and, to a lesser extent in the liver, such suggesting that **NP3** is taken up by phagocytic cells from the
 470 reticuloendothelial system. From the vessel data (Fig. 5-B), we concluded that **NP3** has a long vascular
 471 remanence (> 6h). Therefore, the post-**NP3** MRI scan was scheduled 48h post-injection to allow
 472 sufficient time for nanoparticles elimination from the vascular compartment at the time of scanning.
 473 The long vascular remanence is an advantage for accumulation of the contrast agent in the brain in
 474 presence of a dysfunctional brain blood barrier as encountered in ischemic stroke. On the other hand,
 475 further studies are warranted to further characterize the safety profile of NP3 and in particular its long-
 476 term stability in serum and long-term fate after administration [3].
 477



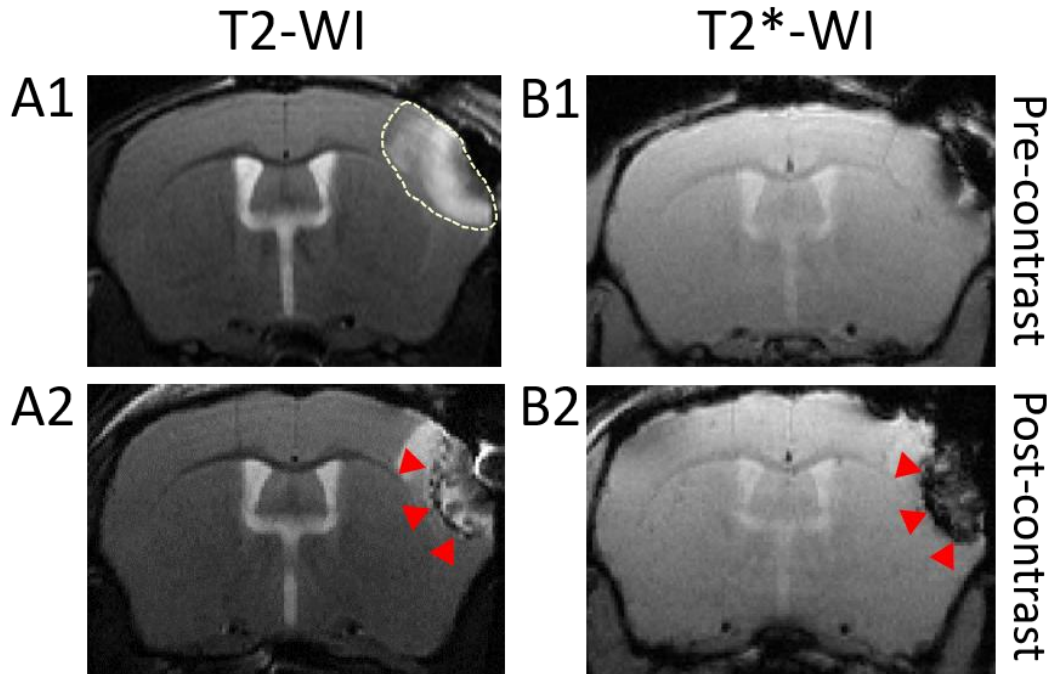
478

479 **Fig 5** Biodistribution and Pharmacokinetic. **A)** **NP3** biodistribution and pharmacokinetic were assessed with a dynamic
 480 sequence in the abdomen. A1: before gadolinium injection and A2: after gadolinium injection, at the end of the dynamic
 481 sequence. Green arrow points to the spleen. **B)** Graph represents the evolution of MR signal intensities due to gadolinium
 482 associated with **NP3** in the spleen and the blood compartment across time after the first pass. Mean \pm SD (n = 4).

483 Multimodal imaging in a mouse model of ischemic stroke

484 Nanoparticle **NP3** was applied as a contrast agent for *in vivo* brain imaging in CX3CR1-GFP/+ mice with
 485 green-fluorescent microglia/macrophages subjected to permanent middle cerebral artery (pMCAo).
 486 The suspension of **NP3** was intravenously injected into the mouse tail vein at the dose of 2 mmol Gd/kg

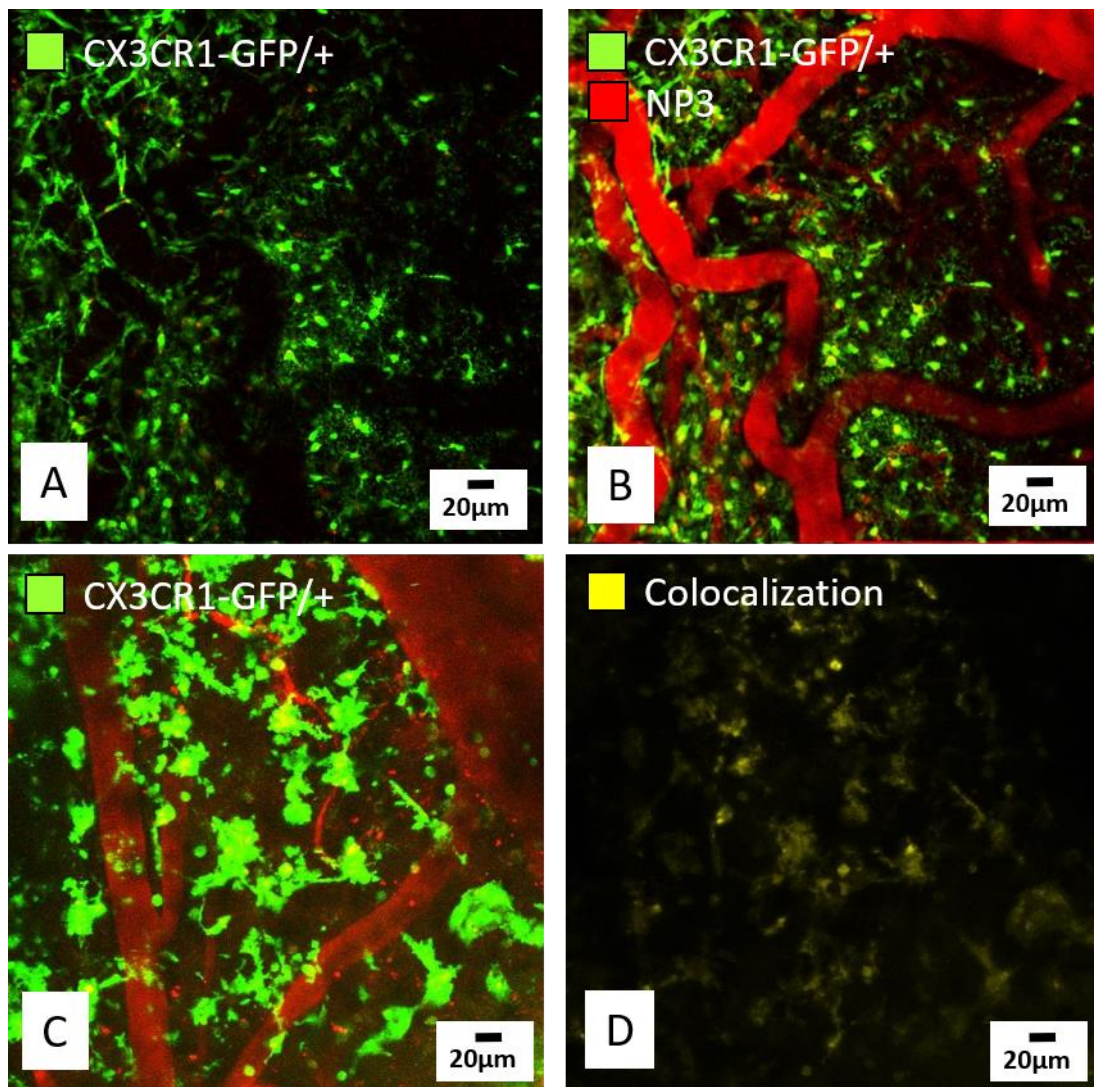
487 and the animal's brain was imaged with MRI and intravital two-photon excitation microscopy (TPEM),
488 before and after the injection of the contrast agent.



489
490 **Fig. 6** *In vivo* NP3-enhanced MRI. **A1, B1**) Pre- and **A2, B2**) post-NP3 injection T₂- and T₂*-weighted images (WI) of a pMCAo
491 mouse brain. The ischemic lesion is seen as a hyperintense signal in T₂-WI (dotted line, A1). Accumulation of the
492 nanoparticles in the ischemic area is characterized by the presence of hypointense signal voids in the lesion on post-NP3 T₂-
493 WI (A2, red arrowheads) and T₂*-WI (B2, red arrowheads).

494 Fig. 6 shows T₂-weighted MR images (T₂-WI) pre- and post-NP3 injection. The ischemic lesion appeared
495 as a hyperintense signal (dotted line) in pre-NP3 T₂-WI (Fig. 6-A1). On the T₂-WI post-contrast images
496 (Fig. 6-A2), signal voids due to the nanoprobe are clearly distinguished inside the lesional area (red
497 arrowheads, ischemic core). Signal voids were also detected within the ischemic core on T₂*-WI (red
498 arrowheads, Fig. 6-B2). This confirms the potential of NP3 as a T₂ and T₂* contrast agent and shows the
499 ability of the probe to accumulate inside the ischemic lesion. The main advantages of this approach
500 compared to nuclear imaging ones is three-fold: first, it allows the imaging at the acute stage of ischemic
501 stroke (3 days post-onset) which is currently not achievable with PET coupled to the administration of
502 TSPO tracers; second, it provides a better spatial resolution in the mouse brain together with accurate
503 morphological lesion depiction; and third, it opens the way to longitudinal tracking of labelled
504 macrophages without the need for additional injection.

505 TPEM imaging offers the possibility to observe the cortical area at the subcellular scale, completing
506 whole-brain MR imaging.

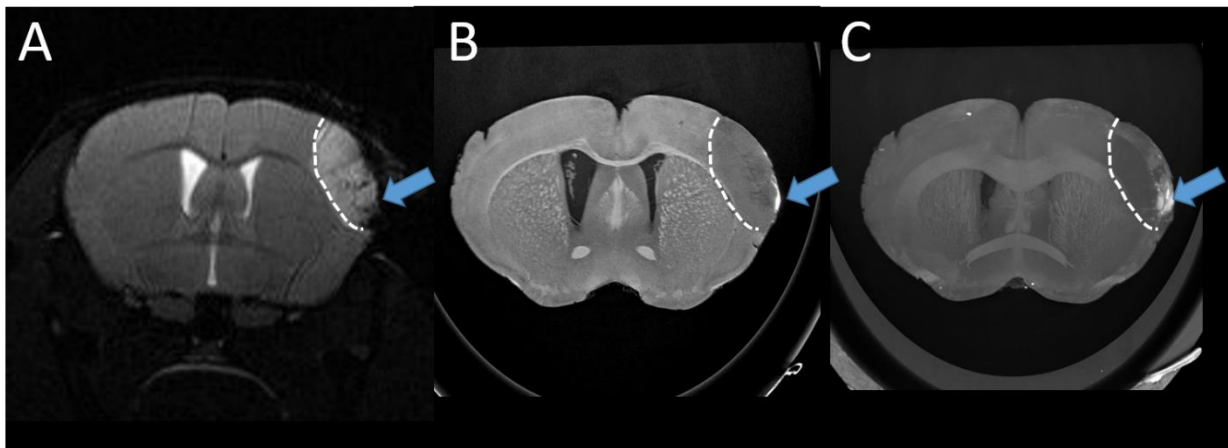


507

508 **Fig. 7** Observation of the **NP3** *in vivo* in different brain compartments using two-photon microscopy. **A, B)** Representative
 509 images of the parenchyma and blood vessels pre- (A) and post-**NP3** injection (B) in a control mouse showing resting CX3CR1-
 510 GFP/+ cells (in green) with ramified morphology. The nanoparticles (in red, B) are observed in the blood vessels immediately
 511 after injection, but not in the brain parenchyma. **C)** In a pMCAo mouse, at the core of the lesion, the nanoparticles are
 512 present in vessels and inside activated CX3CR1-GFP/+ cells. **D)** Nanoparticles are internalized by CX3CR1-GFP/+ cells: yellow
 513 signal corresponds to the colocalization of CX3CR1-GFP/+ cells (green signal in C) and the nanoparticles (red signal in C).

514 In a first series of experiments, CX3CR1-GFP/+ cells were observed by intravital TPEM in the
 515 parenchyma of a control mouse, as well as blood vessels that appear empty on the image before
 516 injection of **NP3** (Fig. 7-A). Immediately after injection, an intense signal was detected in the blood
 517 vessels, indicating the presence of nanoparticles in the blood flow (red signal in Fig. 7-B). Going further,
 518 CX3CR1-GFP/+ mice subjected to pMCAo were imaged with TPEM. When looking at the core of the
 519 ischemic lesion, **NP3** nanoparticles were observed in blood vessels (Fig. 7-C) and an important number
 520 of CX3CR1-GFP/+ cells colocalized with the **NP3** fluorescent signal (yellow signal in Fig. 7-D), suggesting

521 that the nanoparticles are effectively internalized by activated microglial cells and macrophages. Thus,
522 the **NP3**-labeled cells become visible and directly observable in TPEM. Of note, the nanoparticles were
523 still detected with TPEM in the blood vessels 24h post-**NP3** administration (Fig. S7), further confirming
524 the long (> 6 h) vascular remanence of **NP3** observed during the pharmacokinetic study.



525

526 **Fig. 8** *In vivo* T_2 -WI image **A**) and ex vivo phase-contrast computed tomography images **B-C**) for the same pMCAo mouse
527 injected with **NP3**. Hypointense signals on *in vivo* T_2 -WI (**A**, blue arrow) colocalizes with hyperdense signals observed on
528 native image (**B**, blue arrow) and maximum intensity projection (MIP) obtained with phase contrast image (**C**, blue arrow)
529 and corresponding to the presence of Gd in the lesion. Dotted white line delineate the ischemic lesion.

530 In order to ascertain that **NP3** nanoparticle was stable *in vivo* and hence that the GdF_3 core was also
531 found in the brain parenchyma (i.e. in the regions where we detected the red fluorescence of the
532 grafted fluorophore), mice brains have been perfused to wash out the vascular sector, sampled and
533 scanned with synchrotron radiation phase contrast imaging. This innovative technique is based on the
534 imaging of X-ray refraction rather than absorption thus resulting in enhanced contrast of soft tissues
535 while allowing the accurate detection of metal-based contrast agents in the whole brain at microscale-
536 resolution.^{14,34} The gadolinium of **NP3** nanoparticles are clearly seen inside the ischemic lesion as a
537 hyperintense signal that co-localizes with MR signal voids (Fig. 8). In summary, **NP3**-labeled
538 macrophages could be imaged with three complementary imaging modalities, at different scales: MRI
539 ($\sim 100\text{-}\mu\text{m}$), intravital microscopy ($\sim 10\text{-}\mu\text{m}$) and synchrotron x-rays ($\sim 1\text{-}\mu\text{m}$). Such multi-scale approach
540 is crucial in order to decipher the macrophage response at the early stage of ischemic stroke.

541 **Conclusions**

542 A hybrid GdF_3 contrast agent **NP3** was developed and fully characterized for multimodal and multiscale
543 imaging of phagocytic cells. The inorganic core composed of highly crystalline GdF_3 , one of the most

544 stable compounds of gadolinium, shows good properties for MR and X-ray imaging. The PEG layer
545 strongly anchored to the particle through bisphosphonate moieties confers biostability to the
546 nanoparticle. **NP3** has a relatively small hydrodynamic diameter, a long vascular remanence and a
547 negative zeta potential, all properties which are known to be associated with greater uptake by
548 macrophages.^{35,36} *In vitro* cytotoxicity assessments performed on four human cell lines and on bone
549 marrow-derived macrophages revealed no toxic effects. A two-photon active red-fluorophore coupled
550 to the PEG-functionalized nanoparticle provided additive efficient contrast-enhancement properties for
551 *in vivo* two-photon fluorescence imaging with resolution at the molecular scale.

552 The proof-of-concept that **NP3** nanoparticle may be used as a contrast agent targeting phagocytic cells
553 was provided *in vitro* using bone-marrow derived macrophages and *in vivo* in an animal model of
554 ischemic stroke using transgenic CX3CR1-GFP/+ mice. *In vivo* mouse brain MR imaging revealed the
555 accumulation of the particles in the ischemic lesion, which is further confirmed by post-mortem *ex vivo*
556 synchrotron radiation phase contrast imaging. The presence of the particles inside phagocytic cells was
557 evidenced *in vivo* by TEM observations, which indicates the internalization of the contrast agent by
558 cells involved in neuroinflammation. Full validation of the imaging approach in a preclinical study of
559 mice with ischemic stroke is ongoing.³⁷ The next step will be to take advantage of gadolinium for specific
560 imaging with spectral photon counting CT in order to eliminate the need for pre-contrast scanning. Both
561 these imaging approaches are technically challenging due to their lower sensitivity, therefore
562 necessitating further dedicated developments. Nevertheless, our results clearly demonstrate the
563 preclinical potential of hybrid GdF₃ nanoparticles as a promising tool for imaging phagocytic cells in
564 neuroinflammatory diseases with multiscale resolution from macroscopic down to cellular level. Such
565 preclinical imaging tool is crucial to select the immunomodulatory treatments that reach their target
566 and may thus be translated into the clinics.

567 **Authors contributions:** SP and MW designed and supervised the project. SK, FL, FC and SP designed,
568 synthesized and characterized the nanoparticle. YB and CA designed the fluorophore. SK, Y.B, GM, AB
569 and MLI performed the optical characterizations. MM and MLe designed the PEG ligands. AD, MMR and
570 PNM assessed nanotoxicity. IH and OP realized the *in vivo* two-photon imaging and interpreted the
571 data. VH and MW performed the MR imaging experiments and interpreted the data. VH and IH

572 performed the surgeries. SK, VH, IH, FL, SP, MW and OP wrote the article. All authors approved the final
573 version of the manuscript.

574 **Conflicts of interest**

575 There are no conflicts of interest to declare.

576 **Acknowledgements**

577 This study was supported by the Agence Nationale de la Recherche (ANR) (Project Nanobrain, grant #
578 ANR-15-CE18-0026-01). The authors acknowledge the contribution of SFR Biosciences
579 (UMS3444/CNRS, US8/Inserm, ENS de Lyon, UCBL) facilities PLATIM, especially Claire Lionnet, for
580 assistance with the femtosecond laser system. Clémence Gaudin is acknowledged for help with the
581 cytotoxicity evaluations. We thank Lyon's multimodal imaging platform Cermep and the engineers that
582 have helped us perform MR imaging: Jean-Baptiste Langlois and Radu Bolbos. We acknowledge the
583 European Synchrotron Radiation Facility for allocation of beamtime (MD1094) and we would like to
584 thank Emmanuel Brun and Hélène Elleaume for performing acquisitions on Medical Beamline ID17 and
585 phase contrast image reconstruction. The authors acknowledge *Science et Surface* for help with XPS
586 characterization.

587

588

589 **References**

- 590 1 Feigin Valery L., Norrving Bo, and Mensah George A., *Circ. Res.*, 2017, **120**, 439–448.
- 591 2 U. Dirnagl, C. Iadecola and M. A. Moskowitz, *Trends Neurosci.*, 1999, **22**, 391–397.
- 592 3 Q. Wang, X. N. Tang and M. A. Yenari, *J. Neuroimmunol.*, 2007, **184**, 53–68.
- 593 4 A. Ciarmiello, *Eur. J. Nucl. Med. Mol. Imaging*, 2011, **38**, 2198–2201.
- 594 5 C. Corot, K. G. Petry, R. Trivedi, A. Saleh, C. Jonkmanns, J.-F. Le Bas, E. Blezer, M.
- 595 Rausch, B. Brochet, P. Foster-Gareau, D. Balériaux, S. Gaillard and V. Dousset, *Invest.*
- 596 *Radiol.*, 2004, **39**, 619–625.
- 597 6 P. Chhour, P. C. Naha, S. M. O’Neill, H. I. Litt, M. P. Reilly, V. A. Ferrari and D. P.
- 598 Cormode, *Biomaterials*, 2016, **87**, 93–103.
- 599 7 M. N. Bouchlaka, K. D. Ludwig, J. W. Gordon, M. P. Kutz, B. P. Bednarz, S. B. Fain and
- 600 C. M. Capitini, *Oncoimmunology*, 2016, **5**, e1143996.
- 601 8 S. Si-Mohamed, D. Bar-Ness, M. Sigovan, V. Tatard-Leitman, D. P. Cormode, P. C.
- 602 Naha, P. Coulon, L. Rasclé, E. Roessl, M. Rokni, A. Altman, Y. Yagil, L. Bousset and P.
- 603 Douek, *Eur. Radiol. Exp.*, 2018, **2**, 34.
- 604 9 M. L. Cotrina, N. Lou, J. Tome-Garcia, J. Goldman and M. Nedergaard, *Neuroscience*,
- 605 2017, **343**, 483–494.
- 606 10 M. P. Menon and J. James, *J. Chem. Soc. Faraday Trans. 1 Phys. Chem. Condens.*
- 607 *Phases*, 1989, **85**, 2683.
- 608 11 N. Halttunen, F. Lerouge, F. Chaput, M. Vandamme, S. Karpati, S. Si-Mohamed,
- 609 M. Sigovan, L. Bousset, E. Chereul, P. Douek and S. Parola, *Sci. Rep.*, 2019, **9**, 12090.
- 610 12 S. de Reguardati, J. Pahapill, A. Mikhailov, Y. Stepanenko and A. Rebane, *Opt.*
- 611 *Express*, 2016, **24**, 9053–9066.
- 612 13 H. Karatas, S. E. Erdener, Y. Gursoy-Ozdemir, G. Gurer, F. Soylemezoglu, A. K.
- 613 Dunn and T. Dalkara, *J. Cereb. Blood Flow Metab.*, 2011, **31**, 1452–1460.
- 614 14 M. Marinescu, M. Langer, A. Durand, C. Olivier, A. Chabrol, H. Rositi, F.
- 615 Chauveau, T. H. Cho, N. Nighoghossian, Y. Berthezène, F. Peyrin and M. Wiart, *Mol.*
- 616 *Imaging Biol.*, 2013, **15**, 552–559.
- 617 15 F. Mpambani, A. K. O. Åslund, F. Lerouge, S. Nyström, N. Reitan, E. M. Huuse, M.
- 618 Widerøe, F. Chaput, C. Monnerieu, C. Andraud, M. Lecouvey, S. Handrick, S. Prokop,
- 619 F. L. Heppner, P. Nilsson, P. Hammarström, M. Lindgren and S. Parola, *ACS Appl. Bio*
- 620 *Mater.*, 2018, **1**, 462–472.
- 621 16 F. Chaput, F. Lerouge, S. Tusseau-Nenez, P.-E. Coulon, C. Dujardin, S. Denis-
- 622 Quanquin, F. Mpambani and S. Parola, *Langmuir*, 2011, **27**, 5555–5561.
- 623 17 EP2445838 (A1), 2009.
- 624 18 E. Ringe, R. P. Van Duyne and L. D. Marks, *Nano Lett.*, 2011, **11**, 3399–3403.

- 625 19 S. Kachbi-Khelfallah, M. Monteil, M. Cortes-Clerget, E. Migianu-Griffoni, J.-L.
626 Pirat, O. Gager, J. Deschamp and M. Lecouvey, *Beilstein J. Org. Chem.*, 2016, **12**,
627 1366–1371.
- 628 20 Z.-Y. Yang, S.-L. Luo, H. Li, S.-W. Dong, J. He, H. Jiang, R. Li and X.-C. Yang, *RSC*
629 *Adv*, 2014, **4**, 59965–59969.
- 630 21 L. Sandiford, A. Phinikaridou, A. Protti, L. K. Meszaros, X. Cui, Y. Yan, G.
631 Frodsham, P. A. Williamson, N. Gaddum, R. M. Botnar, P. J. Blower, M. A. Green and
632 R. T. M. de Rosales, *ACS Nano*, 2013, **7**, 500–512.
- 633 22 S. Redon, J. Massin, S. Pouvreau, E. De Meulenaere, K. Clays, Y. Queneau, C.
634 Andraud, A. Girard-Egrot, Y. Bretonnière and S. Chambert, *Bioconjug. Chem.*, 2014,
635 **25**, 773–787.
- 636 23 Z. Varga, J. Mihály, Sz. Berényi and A. Bóta, *Eur. Polym. J.*, 2013, **49**, 2415–2421.
- 637 24 R. Lemke, *Synthesis*, 1974, **1974**, 359–361.
- 638 25 J. Massin, W. Dayoub, J.-C. Mulatier, C. Aronica, Y. Bretonnière and C. Andraud,
639 *Chem. Mater.*, 2011, **23**, 862–873.
- 640 26 J. Massin, A. Charaf-Eddin, F. Appaix, Y. Bretonnière, D. Jacquemin, B. van der
641 Sanden, C. Monnereau and C. Andraud, *Chem. Sci.*, 2013, **4**, 2833.
- 642 27 R. Huisgen, *Angew. Chem. Int. Ed. Engl.*, 1963, **2**, 565–598.
- 643 28 H. J. Benyettou F, *J. Bioanal. Biomed.*, 2012, **04**, 39.
- 644 29 J. F. Moulder and J. Chastain, Eds., *Handbook of X-ray photoelectron*
645 *spectroscopy: a reference book of standard spectra for identification and*
646 *interpretation of XPS data*, Perkin-Elmer Corporation, Eden Prairie, Minn, Update.,
647 1992.
- 648 30 N. Boens, W. Qin, N. Basarić, J. Hofkens, M. Ameloot, J. Pouget, J.-P. Lefèvre, B.
649 Valeur, E. Gratton, M. vandeVen, N. D. Silva, Y. Engelborghs, K. Willaert, A. Sillen, G.
650 Rumbles, D. Phillips, A. J. W. G. Visser, A. van Hoek, J. R. Lakowicz, H. Malak, I.
651 Gryczynski, A. G. Szabo, D. T. Krajcarski, N. Tamai and A. Miura, *Anal. Chem.*, 2007,
652 **79**, 2137–2149.
- 653 31 C. Xu and W. W. Webb, *JOSA B*, 1996, **13**, 481–491.
- 654 32 N. S. Makarov, J. Campo, J. M. Hales and J. W. Perry, *Opt. Mater. Express*, 2011,
655 **1**, 551–563.
- 656 33 S. Liu, J.-C. Brisset, J. Hu, E. M. Haacke and Y. Ge, *J. Magn. Reson. Imaging*, 2018,
657 **47**, 621–633.
- 658 34 J. Albers, S. Pacilé, M. A. Markus, M. Wiart, G. Vande Velde, G. Tromba and C.
659 Dullin, *Mol. Imaging Biol.*, 2018, **20**, 732–741.
- 660 35 C. Corot, P. Robert, J.-M. Idée and M. Port, *Adv. Drug Deliv. Rev.*, 2006, **58**, 1471–
661 1504.
- 662 36 E. Fröhlich, *Int. J. Nanomedicine*, 2012, **7**, 5577–5591.

663 37 V. Hubert, I. Hristovska, S. Karpati, S. Benkeder, C. Dumot, C. Amaz, N.
664 Chounlamountri, C. Watrin, J.-C. Comte, F. Chauveau, E. Brun, F. Lerouge, S. Parola,
665 O. Pascual and M. Wiart, .Paper on preparation

- 666
667
668 1. Zinnhardt, B., et al., Theranostics, 2018. **8**(10): p. 2603-2620.
669 2. Schirra, C.O., et al., Contrast Media Mol Imaging, 2014. **9**(1): p. 62-70.
670 3. Tamion, A., et al., Nano Research, 2016. **9**(8): p. 2398-2410.

671
672